

## Mild Deoxygenation of Sulfoxides over Plasmonic Molybdenum Oxide Hybrid with Dramatic Activity Enhancement under Visible Light

Yasutaka Kuwahara, Yukihiro Yoshimura, Kohei Haematsu, and Hiromi Yamashita

*J. Am. Chem. Soc.*, **Just Accepted Manuscript** • DOI: 10.1021/jacs.8b04711 • Publication Date (Web): 17 Jun 2018

Downloaded from <http://pubs.acs.org> on June 18, 2018

### Just Accepted

“Just Accepted” manuscripts have been peer-reviewed and accepted for publication. They are posted online prior to technical editing, formatting for publication and author proofing. The American Chemical Society provides “Just Accepted” as a service to the research community to expedite the dissemination of scientific material as soon as possible after acceptance. “Just Accepted” manuscripts appear in full in PDF format accompanied by an HTML abstract. “Just Accepted” manuscripts have been fully peer reviewed, but should not be considered the official version of record. They are citable by the Digital Object Identifier (DOI®). “Just Accepted” is an optional service offered to authors. Therefore, the “Just Accepted” Web site may not include all articles that will be published in the journal. After a manuscript is technically edited and formatted, it will be removed from the “Just Accepted” Web site and published as an ASAP article. Note that technical editing may introduce minor changes to the manuscript text and/or graphics which could affect content, and all legal disclaimers and ethical guidelines that apply to the journal pertain. ACS cannot be held responsible for errors or consequences arising from the use of information contained in these “Just Accepted” manuscripts.

# Mild Deoxygenation of Sulfoxides over Plasmonic Molybdenum Oxide Hybrid with Dramatic Activity Enhancement under Visible Light

Yasutaka Kuwahara,<sup>†,‡</sup> Yukihiro Yoshimura,<sup>†</sup> Kohei Haematsu,<sup>†</sup> and Hiromi Yamashita<sup>\*,†,‡</sup>

<sup>†</sup> Division of Materials and Manufacturing Science, Graduate School of Engineering, Osaka University, 2-1 Yamadaoka, Suita, Osaka 565-0871, Japan

<sup>‡</sup> Unit of Elements Strategy Initiative for Catalysts & Batteries (ESICB), Kyoto University, Katsura, Kyoto 615-8520, Japan

**KEYWORDS:** deoxygenation, sulfoxides, hydrogen molybdenum bronze, surface plasmon resonances, heterogeneous catalyst

**ABSTRACT:** Harvesting solar light to boost commercially important organic synthesis still remains a challenge. Coupling of conventional noble metal catalysts with plasmonic oxide materials which exhibit intense plasmon absorption in the visible light region is a promising option for efficient solar energy utilization in catalysis. Herein we for the first time demonstrate that plasmonic hydrogen molybdenum bronze coupled with Pt nanoparticles (Pt/H<sub>x</sub>MoO<sub>3-y</sub>) shows a high catalytic performance in the deoxygenation of sulfoxides with 1 atm H<sub>2</sub> at room temperature, with dramatic activity enhancement under visible light irradiation relative to dark condition. The plasmonic molybdenum oxide hybrids with strong plasmon resonance peaks pinning at around 556 nm are obtained *via* a facile H-spillover process. Pt/H<sub>x</sub>MoO<sub>3-y</sub> hybrid provides excellent selectivity for the deoxygenation of various sulfoxides as well as pyridine *N*-oxides, in which drastically improved catalytic efficiencies are obtained under the irradiation of visible light. Comprehensive analyses reveal that oxygen vacancies massively introduced *via* a H-spillover process are the main active sites, and reversible redox property of Mo atoms and strong plasmonic absorption play key roles in this reaction. The catalytic system works under extremely mild conditions and can boost the reaction by the assist of visible light, offering an ultimately greener protocol to produce sulfides from sulfoxides. Our findings may open up a new strategy for designing plasmon-based catalytic systems that can harness visible light efficiently.

## 1. INTRODUCTION

Harvesting and converting abundant sunlight to drive chemical reactions is of immense interests in terms of solar energy conversion and environmental consideration, especially for heterogeneous catalysis that has been industrially implemented in a large-scale. Heterogeneous photo-catalysis based on surface plasmonic resonance (SPR) opens up a promising alternative technology in this field since the plasmon resonance frequency predominantly appear in visible- to near-infrared (NIR) light region.<sup>1-5</sup> Recent studies have witnessed that the SPR of noble-metal-based plasmonic materials (e.g. Au and Ag) enables to boost catalytic performance in various important organic transformations, including oxidation of aromatic alcohols,<sup>6</sup> reduction of ketones, epoxides, and azo compounds on Au nanoparticles (NPs),<sup>7</sup> reduction of nitroaromatics on Ag or Au NPs,<sup>4, 8-9</sup> and epoxidation of ethylene on Ag NPs.<sup>10</sup> Bimetallic alloy NPs composed of plasmonic NPs and other catalytically active noble metals (e.g. Pd) have been found to be efficient plasmon-catalysts to drive Suzuki coupling reactions<sup>11-13</sup> and oxidation of benzylamine<sup>12</sup> by the assist of visible light, mainly due to the plasmon-induced generation of energetic electrons at the surface of active metals.

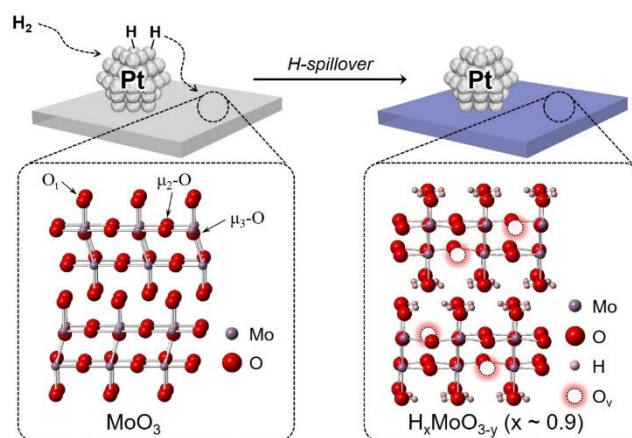
Recently, heavily doped semiconductors such as transparent conducting oxide (TCO)<sup>14-15</sup> and transition metal oxides/chalcogenides<sup>16-17</sup> have emerged as a new family of plasmonic materials alternative to conventional noble metals. Plasmonic features of these materials can be controlled by tuning the concentration of free carriers (electrons and holes) in the crystal structure, which can be accomplished by heavily doping aliovalent heteroatoms or lattice vacancies.<sup>14, 18-20</sup> Hydrogen doping is a rational protocol to achieve plasmon resonances in semiconductors, since it induces intrinsic defects and concurrently introduces massive electrons to the given host structures without extensive structural expansion, thus yielding sufficient delocalized electrons to support the plasmon resonance in the spectrum of visible light region.<sup>21-22</sup> Among this material family, H-doped molybdenum oxides (H<sub>x</sub>MoO<sub>3</sub>), namely hydrogen molybdenum bronze, can be regarded as a promising plasmonic platforms for the design of light-harvesting catalytic system because of i) the appearance of intense plasmon absorption in the visible light to near-infrared (NIR) region due to high dopant concentration (> 10<sup>21</sup> cm<sup>-3</sup>) and ii) the intercalated H atoms and concurrently injected free electrons in the MoO<sub>3</sub> matrices that are reversibly exchangeable during redox events.<sup>23-24</sup> Owing to

the high energy of the  $H_xMoO_3$  SPR relative to other semiconductor SPRs, it has currently found diverse applications in the areas of bioimaging, sensing, optical devices, and catalysis.<sup>25-28</sup> Previous studies on the catalytic applications of plasmonic  $H_xMoO_3$  have been limited to the dehydrogenation of ammonia borane ( $NH_3BH_3$ ), which inherently proceeds even at ambient conditions.<sup>23, 29</sup> Plasmonic molybdenum oxide hybrids consisting of  $H_xMoO_3$  and active metal catalysts (e.g. Pd) can provide more extended catalytic opportunities, such as *p*-nitrophenol reduction<sup>22</sup> and Suzuki coupling reactions,<sup>30</sup> in which reaction efficiencies are significantly improved under the irradiation of visible light; however, application to more practically important organic transformations has not been accomplished yet. The intercalated dopants and the defect sites ( $H^+$  and oxygen defects) massively introduced in the  $MoO_3$  framework may offer unique reactivities towards surrounding reactants; for example, Mu *et al.* have claimed that the Mo–OH group on the  $H_xMoO_3$  surface play a key role in the selective C–O bond cleavage of biomass-derived tetrahydrofurfuryl alcohol,<sup>31</sup> and other reports have demonstrated that oxygen defects in  $MoO_{3-x}$  suboxide are responsible for the active sites in the hydrodeoxygenation of ketones,<sup>32</sup> while these reactions have been achieved under harsh reaction conditions ( $\sim 400$  °C). Combination of plasmonic property and unique catalytic properties of hydrogen molybdenum bronze is expected to offer unprecedented catalytic opportunities under light irradiation conditions, which may open up a new avenue for the design of plasmon-based heterogeneous catalysts that can harness visible light efficiently.

Herein we for the first time demonstrate that hydrogen-doped  $MoO_3$  coupled with Pt NPs shows a high catalytic performance in the deoxygenation of sulfoxides with 1 atm  $H_2$  at room temperature, with dramatic activity enhancement under visible light irradiation relative to dark condition. Deoxygenation of sulfoxides to sulfides is a fundamental and important reaction for organic synthesis and biochemistry.<sup>33-34</sup> The deoxygenation of sulfoxides typically requires stoichiometric amounts of reducing agents such as phosphines,<sup>35</sup> boranes,<sup>36</sup> silanes,<sup>37</sup> and alcohols,<sup>38</sup> which, however, suffer from the use of toxic reagents and the production of undesirable by-products as well as low atom-efficiency. Alternatively, the catalytic deoxygenation of sulfoxides using molecular  $H_2$  as the most greener reducing agent has been examined using  $MoO_2Cl_2$ ,<sup>33</sup> Pd/C,<sup>39</sup> Pt- $MoO_x/TiO_2$ ,<sup>40</sup> and Pt/ $V_{(1-x)}Cr_x$ -Hol,<sup>41</sup> but they require harsh reaction conditions including high  $H_2$  pressure ( $> 7$  atm). Recently, Mitsudome *et al.* demonstrated catalytic deoxygenation of sulfoxides under atmospheric  $H_2$  pressure using Ru/ $TiO_2$  at 100 °C;<sup>42</sup> however, there has been no report on the deoxygenation of sulfoxides using 1 atm  $H_2$  at room temperature. The present catalytic system works under extremely mild conditions and can boost the deoxygenation of sulfoxide by the assist of visible light, offering an ultimately greener protocol to produce sulfides from sulfoxides.

## 2. RESULTS AND DISCUSSION

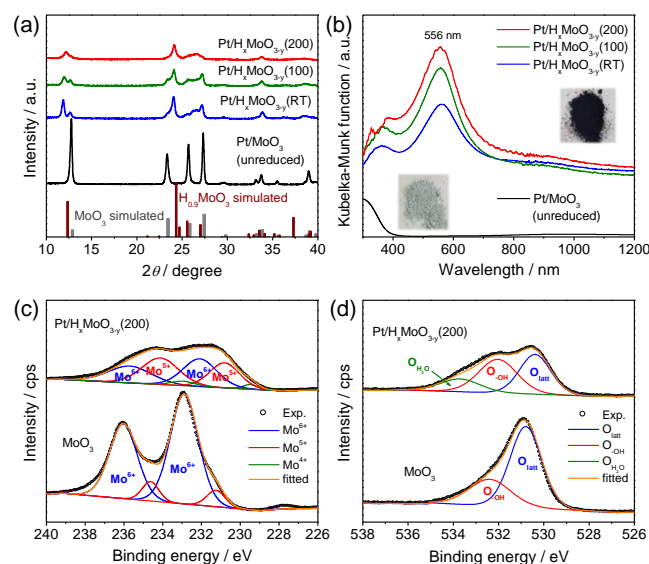
**Characterization of plasmonic molybdenum oxide hybrid.** The synthesis of plasmonic molybdenum oxide coupled with Pt NPs ( $Pt/H_xMoO_{3-y}$ ) was performed via a H-spillover process (Figure 1).<sup>22</sup>  $\alpha$ - $MoO_3$  containing Pt ions was reduced in a flow of  $H_2$  at controlled temperature (R.T., 100 °C, and 200 °C) to yield a dark blue powder. Here the dopants ( $H^+$ ) and free electrons are injected into  $MoO_3$  matrices through *in-situ* formed Pt NPs, causing a rapid dissociation of molecular  $H_2$  over Pt surface ( $H_2 \rightarrow 2H^+ + 2e^-$ ), in which the  $H^+$  dopant levels and oxygen defect densities can easily be modulated by the reduction temperature. The H-spillover process was verified by hydrogen temperature-programmed reduction results ( $H_2$ -TPR, Figure S1).  $MoO_3$  could be reduced at below 100 °C when coupled with Pt NPs, while pristine  $MoO_3$  was hardly reduced by molecular  $H_2$  up to 550 °C. The molar ratio of H atoms consumed per mole of Pt atoms contained in the catalyst (H/Pt) was determined to be 885, whereas Pt/ $SiO_2$  as a comparative sample gave H/Pt molar ratio of 4.2, demonstrating an intercalation of massive amount of hydrogen atoms into  $MoO_3$  matrices via a H-spillover process.



**Figure 1.** Schematic illustration of the formation of hydrogen molybdenum bronzes ( $H_xMoO_{3-y}$ ) via a H-spillover process. Overview of the crystal structures of (left) orthorhombic  $MoO_3$  and (right) monoclinic  $H_xMoO_{3-y}$  ( $x \sim 0.9$ ), showing OH and  $OH_2$  groups predominantly located at terminal oxygen atoms ( $O_t$ ) and oxygen vacancies ( $O_v$ ) predominantly formed at  $\mu_2$ -bridging oxygen sites ( $\mu_2-O$ ).

The intercalation of hydrogen atoms into  $MoO_3$  matrices is known to yield a class of  $H_xMoO_3$  ( $0 < x \leq 2$ ) along with partial reduction of Mo ions.<sup>43-46</sup> The peaks at 12.7, 25.7, and 38.92° for the untreated Pt/ $MoO_3$  correspond to the (020), (040), and (060) crystal planes of orthorhombic  $\alpha$ - $MoO_3$  (PDF#5-0508). XRD patterns of Pt/ $H_xMoO_{3-y}$  reduced under  $H_2$  condition are predominantly indexed to monoclinic  $H_{0.9}MoO_3$  phase (PDF#53-1024), which contains H atoms at the interlayer positions of double layers of  $MoO_6$  octahedra,<sup>45-46</sup> crystallographically evidencing the intercalation of H atoms into  $MoO_3$  matrices upon  $H_2$  reduction (Figure 2a). Shift of the position of (020) basal plane toward smaller angle indicates the expansion of interlayer spacings due to the intercalation of  $H^+$  ions at the interstitial sites. With the rise of reduction temperature, the relative

proportion of  $\text{MoO}_3$  decreases, indicating a gradual transformation of  $\alpha\text{-MoO}_3$  to  $\text{H}_{0.9}\text{MoO}_3$  phase at elevated temperatures. It is also noteworthy that peak intensities of  $\text{H}_{0.9}\text{MoO}_3$  decreases with the rise of reduction temperature. This may be interpreted by the perturbation of  $\text{H}_{0.9}\text{MoO}_3$  crystal structure associated with the introduction of oxygen vacancies and distortion of  $\text{MoO}_6$  octahedra.<sup>22</sup> After  $\text{H}_2$  reduction,  $\text{Pt}/\text{H}_x\text{MoO}_{3-y}$  samples exhibit strong absorption in the visible to NIR region with an intense SPR peak pinning at around 556 nm, while the unreduced  $\text{Pt}/\text{MoO}_3$  only shows an absorption below 400 nm owing to the semiconductive nature (Figure 2b). As  $\text{H}_2$  reduction temperature increases, a blue shift of the plasmonic wavelength from 564 to 556 nm is observed, together with an intensification of the absorption peaks, which is due to the increased concentration of free carriers in the  $\text{MoO}_3$  host structure.<sup>18, 22</sup> However, further rise of reduction temperature to 300 °C leads to the quenching of plasmonic absorption due to the structural deformation into amorphous  $\text{MoO}_{3-x}$  suboxide (Figure S2).



**Figure 2.** (a) Powder XRD patterns, (b) UV-vis-NIR diffuse reflectance spectra for the  $\text{Pt}/\text{H}_x\text{MoO}_{3-y}$  hybrids reduced at varied temperatures and for the unreduced  $\text{Pt}/\text{MoO}_3$ . (c) Mo 3d XPS spectra and (d) O 1s XPS spectra for the  $\text{Pt}/\text{H}_x\text{MoO}_{3-y}(200)$  and for the pristine  $\text{MoO}_3$ .

X-ray photoelectron spectroscopy (XPS) is used to confirm the oxidation state of the samples. For the series of  $\text{Pt}/\text{H}_x\text{MoO}_{3-y}$  samples, Mo species with lower oxidation states appear in Mo 3d XPS spectra ( $\text{Mo}^{5+}$ ; BE at 230.8 and 234.0 eV,  $\text{Mo}^{4+}$ ; BE at 229.5 and 233.0 eV), while  $\text{Mo}^{6+}$  species (BE at 235.8 and 232.1 eV) are dominantly observed for pristine  $\text{MoO}_3$  (Figure 2c), indicative of partial reduction of Mo species upon  $\text{H}_2$  reduction.<sup>47</sup> Based on fitting analysis, the average oxidation number ( $N_{\text{oxi}}$ ) is found to gradually reduce from 5.89 to 5.42 along with the rise of reduction temperature from R.T. to 200 °C (for detail, see Figure S3, Table S1). Such a change in the oxidation state of Mo species was also corroborated by *in-situ* X-ray absorption

fine structure (XAFS) measurement for Mo K-edge in a flow of  $\text{H}_2$ , in which a gradual shift of the absorption edge toward a lower energy region and a shrinkage of Mo–O bond associated with the phase transition during  $\text{H}_2$  reduction were directly observed (Figure S4).<sup>22-23</sup> Figure 2d shows O 1s XPS spectra of the samples. Pristine  $\text{MoO}_3$  exhibits the peaks ascribed to lattice O atoms ( $\text{O}_{\text{lat}}$ ) at 530.8 eV and small portion of –OH groups ( $\text{O}_{\text{OH}}$ ) at 532.4 eV. The peak for the  $\text{O}_{\text{OH}}$  species drastically increases in intensity after  $\text{H}_2$  reduction at 200 °C, evidencing the emergence of Mo–OH bond.<sup>48</sup> Furthermore, a small peak appeared at 533.7 eV can be assigned to  $-\text{OH}_2$  groups coordinated to Mo atoms ( $\text{O}_{\text{H}_2\text{O}}$ ). The proportion of  $(\text{O}_{\text{OH}} + \text{O}_{\text{H}_2\text{O}})/\text{O}_{\text{total}}$  increased in the order of pristine  $\text{MoO}_3$  (30 at%) <  $\text{Pt}/\text{H}_x\text{MoO}_{3-y}(\text{RT})$  (55 at%) <  $\text{Pt}/\text{H}_x\text{MoO}_{3-y}(100)$  (58 at%) <  $\text{Pt}/\text{H}_x\text{MoO}_{3-y}(200)$  (59 at%), again evidencing a higher degree of  $\text{H}^+$ -intercalation at elevated reduction temperatures (for detail, see Figure S3, Table S1). In addition, Pt species are found to dominantly exist as metallic  $\text{Pt}^0$  NPs (average diameter = ca. 2.2 nm) after  $\text{H}_2$  reduction (see Figure S5). These results evidence that, during  $\text{H}_2$  reduction, the H atoms are injected into  $\text{MoO}_3$  matrices through *in-situ* formed  $\text{Pt}^0$  NPs as windows, and are then inserted at interlayer positions of layered  $\text{MoO}_3$  framework by coordinating with terminal oxygen atoms ( $\text{O}_t$ ) through  $\text{Mo}^{5+}\text{–OH}$  bond (see Figure 1).<sup>46, 49-50</sup> The formation of such –OH sites was verified by temperature-programmed desorption measurement using  $\text{NH}_3$  as a probe molecule ( $\text{NH}_3\text{-TPD}$ , Figure S6). Reduced  $\text{Pt}/\text{H}_x\text{MoO}_{3-y}$  hybrids showed desorption peaks of  $\text{NH}_3$  in the range of 200–600 °C, whereas unreduced  $\text{Pt}/\text{MoO}_3$  showed no peak in this range, proving the emergence of acid sites associated with –OH groups in the  $\text{MoO}_3$  framework upon the  $\text{H}_2$  reduction treatment. Such a structural alteration upon  $\text{H}^+$ -intercalation results in a decreased intensity of Raman peaks of  $\text{MoO}_3$  (Figure S7), suggesting the concomitant formation of oxygen vacancies ( $\text{O}_v$ ). In order to quantify the amounts of intercalated  $\text{H}^+$  and oxygen vacancies formed upon  $\text{H}_2$  reduction, thermogravimetric (TG) analysis was carried out in either  $\text{N}_2$  or air gas environment. Based on the weight changes associated with the release of intercalated  $\text{H}^+$  (in  $\text{N}_2$  environment) and the filling of  $\text{O}_v$  (in air environment), the stoichiometric compositions of the series of the samples were determined to be  $\text{Pt}/\text{H}_{0.19}\text{MoO}_{2.98}(\text{RT})$ ,  $\text{Pt}/\text{H}_{0.50}\text{MoO}_{2.97}(100)$ , and  $\text{Pt}/\text{H}_{0.82}\text{MoO}_{2.49}(200)$ , respectively (Table 1) (for detailed TG analysis, see Figure S8).<sup>43, 47, 51</sup> This result ascertains the introduction of increased amounts of  $\text{H}^+$  and  $\text{O}_v$  sites at elevated reduction temperatures, which are well coincided with the results shown above. It is also worth noting that there was no significant structural variation upon the  $\text{H}_2$  reduction treatment in terms of surface area and pore volume, despite such considerable changes in crystal structure and chemical composition (Table 1).



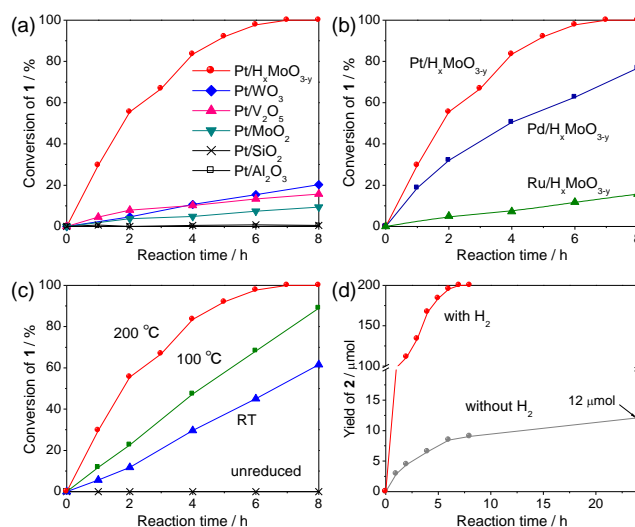
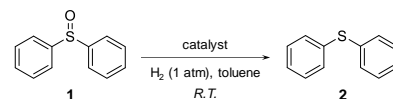
**Table 1. Textural and compositional parameters of Pt/H<sub>x</sub>MoO<sub>3-y</sub> samples**

| Samples                                    | Reduction Temp. (°C) | N <sub>2</sub> physisorption                      |  | TG analysis                                      |                                     |
|--|----------------------|---|--|--|-------------------------------------|
|  |                      | S <sub>BET</sub> <sup>a</sup> (m <sup>2</sup> /g) | V <sub>total</sub> <sup>b</sup> (cm <sup>3</sup> /g) | Concentration of intercalated H <sup>+</sup> (x) | Concentration of O <sub>v</sub> (y) |
| Pt/MoO <sub>3</sub> (unreduced)            | None                 | 7.5   | 0.052  | 0.0  | 0.0                                 |
| Pt/H <sub>x</sub> MoO <sub>3-y</sub> (RT)  | RT                   | 7.6   | 0.057  | 0.19   | 0.02                                |
| Pt/H <sub>x</sub> MoO <sub>3-y</sub> (100) | 100                  | 7.1   | 0.046  | 0.50   | 0.03                                |
| Pt/H <sub>x</sub> MoO <sub>3-y</sub> (200) | 200                  | 7.0   | 0.047  | 0.82   | 0.51                                |

<sup>a</sup> Determined by the BET method by using adsorption data ranging from  $p/p_0 = 0.05$  to  $0.30$ . <sup>b</sup> Reported at  $p/p_0 = 0.99$ .

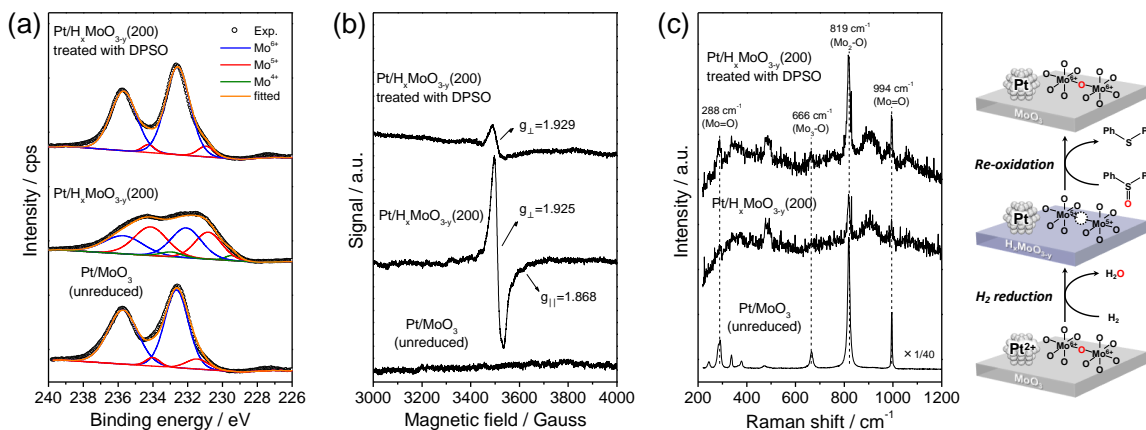
**Deoxygenation of sulfoxide.** The catalytic performance of the samples was initially assessed in the deoxygenation of diphenyl sulfoxide (**1**) as a model substrate at room temperature under a flow of 1 atm H<sub>2</sub> in the dark condition (**Scheme 1**). Toluene was chosen as a suitable solvent to achieve a high catalytic efficiency. A better catalytic efficiency was obtained with non-polar solvents and the use of polar solvent resulted in a poor catalytic efficiency (for the effect of solvent, see **Figure S9**). Among Pt NP catalyst supported on metal oxides (metal loading was fixed to be 0.5 wt%), Pt/H<sub>x</sub>MoO<sub>3-y</sub> exhibited the highest catalytic activity, affording diphenyl sulfide (**2**) in >99% yield in 7 h of reaction (**Figure 3a**), corresponding to a turnover number (TON) of 160 with respect to the total number of Pt atoms in the catalyst. Considering the reaction conditions implemented in this study, this value is superior to those obtained with previously reported catalysts requiring high temperature and high H<sub>2</sub> pressure (Pd/C: TON 50 (at 90 °C, 79 atm));<sup>39</sup> Pt/V<sub>(1-x)</sub>Cr<sub>x</sub>-Hol: TON 230 (at 100 °C, 1 atm);<sup>41</sup> Ru/TiO<sub>2</sub>: TON 500 (at 100 °C, 1 atm)<sup>42</sup>. In fact, Pd/C (5% Pd) catalyst<sup>39</sup> was totally inactive in this reaction under the conditions implemented in this study. Ru/TiO<sub>2</sub> catalyst reported by Mitsudome *et al.*<sup>42</sup> exhibited an activity under the identical reaction conditions, giving 97% conversion within 2 h of reaction; however, TON with respect to the total number of Ru atoms was calculated to be 6.5 (TOF = 3.3 h<sup>-1</sup>), while that afforded by Pt/H<sub>x</sub>MoO<sub>3-y</sub>(200) catalyst was 160 (TOF = 23 h<sup>-1</sup>), clearly demonstrating that the activity of Pt/H<sub>x</sub>MoO<sub>3-y</sub>(200) catalyst is superior to those obtained with previously reported catalysts. Pt/SiO<sub>2</sub> and Pt/Al<sub>2</sub>O<sub>3</sub> were inactive for this reaction, indicating that Pt NPs are not the main active sites in this reaction. The activity of Pt supported on H<sub>x</sub>MoO<sub>3-y</sub> was higher than those of Pd and Ru supported on H<sub>x</sub>MoO<sub>3-y</sub> (**Figure 3b**). The order of efficiency of the metals can be associated with the ability of the metals to dissociate H<sub>2</sub>, i.e., Pt and Pd NPs dissociates H<sub>2</sub> with lower activation energy than Ru NPs, thereby reducing the total activation energy required for this reaction. Plasmonic molybdenum oxide nanosheet prepared by solvothermal method<sup>23</sup> exhibited a slight activity, giving 2.3% conversion in 8 h, which is due to the absence of Pt NPs acting as H<sub>2</sub> dissociation sites.

### Scheme 1 Deoxygenation of diphenyl sulfoxide to diphenyl sulfide with 1 atm H<sub>2</sub> at room temperature



**Figure 3.** Time course in the deoxygenation of **1** over (a) various Pt-loaded oxide catalysts (reduction Temp. = 200 °C), (b) M/H<sub>x</sub>MoO<sub>3-y</sub> catalysts (M = Pt, Pd, Ru) (reduction Temp. = 200 °C), and (c) Pt/H<sub>x</sub>MoO<sub>3-y</sub> catalysts reduced at varied temperature. (d) Time course of the yield of **2** over Pt/H<sub>x</sub>MoO<sub>3-y</sub>(200) catalyst with or without H<sub>2</sub>. Reaction conditions: catalyst (0.05 g), **1** (0.2 mmol), toluene (10 mL), room temperature, H<sub>2</sub> bubbling (10 mL/min), in the dark.

Pt supported on easily reducible metal oxides such as Pt/WO<sub>3</sub> and Pt/V<sub>2</sub>O<sub>5</sub> exhibited moderate activities (**Figure 3a**), suggesting the significance of defect sites on oxide supports. It was found that the catalytic activity of the Pt/H<sub>x</sub>MoO<sub>3-y</sub> increases as the reduction temperature increases (**Figure 3c**). Considering the correlation between the observed catalytic activities and the stoichiometry of H<sup>+</sup> or O<sub>v</sub> determined by TG analysis, oxygen defect sites would be the main active sites for this reaction (for the correlations between the stoichiometry of H<sup>+</sup> or O<sub>v</sub> and catalytic activities, see **Figure S10**). To verify the above hypothesis, the deoxygenation reaction was carried out in the absence of H<sub>2</sub> gas. It was found that 12 μmol of **2** was yielded after 24 h of reaction per 50 mg of catalyst even in the absence of H<sub>2</sub> (**Figure 3d**). Pt/H<sub>x</sub>MoO<sub>3-y</sub>(200) treated with **1** in toluene under an Ar atmosphere at room

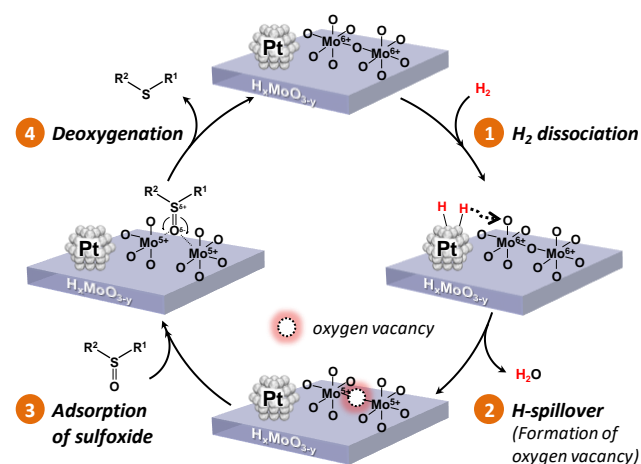


**Figure 4.** (a) Mo 3d XPS spectra, (b) electron spin resonance (ESR) spectra, and (c) Raman spectra of as-synthesized Pt/MoO<sub>3</sub>, Pt/H<sub>x</sub>MoO<sub>3-y</sub>(200) and the retrieved Pt/H<sub>x</sub>MoO<sub>3-y</sub>(200) after the treatment with diphenyl sulfoxide (DPSO) in toluene under an Ar gas atmosphere at room temperature for 24 h.

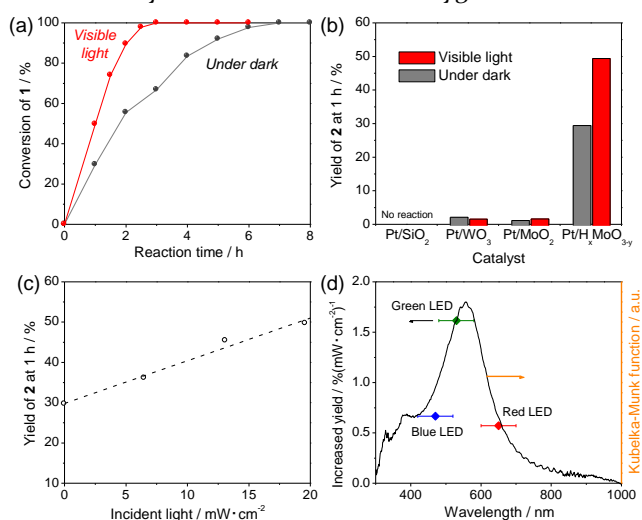
temperature for 24 h was further analyzed by XPS, electron spin resonance (ESR), and Raman spectroscopy analyses. As aforementioned, in Mo 3d XPS spectrum, Pt/H<sub>x</sub>MoO<sub>3-y</sub>(200) show peaks attributable to Mo species with lower oxidation states, while as-synthesized Pt/MoO<sub>3</sub> dominantly exhibits peaks attributable to Mo<sup>6+</sup> species. After treatment of Pt/H<sub>x</sub>MoO<sub>3-y</sub>(200) with **1** in an Ar environment for 24 h, peaks attributable to Mo<sup>6+</sup> species were again dominantly emerged (**Figure 4a**). In ESR spectrum of Pt/H<sub>x</sub>MoO<sub>3-y</sub>(200), *g* values typical of five-coordinated Mo<sup>5+</sup> species (*g*<sub>⊥</sub> = 1.925 and *g*<sub>∥</sub> = 1.868) are observed,<sup>52-53</sup> while such a peak is not observable for the as-synthesized Pt/MoO<sub>3</sub> having only Mo<sup>6+</sup> species. The ESR signal attributable to five-coordinated Mo<sup>5+</sup> species was obviously diminished after the treatment with **1** in Ar atmosphere, evidencing the re-oxidation of the reduced Mo species to Mo<sup>6+</sup> (**Figure 4b**). In Raman spectrum of Pt/H<sub>x</sub>MoO<sub>3-y</sub>(200), the Raman peak assignable to doubly coordinated bridging oxygen (Mo<sub>2</sub>-O)<sup>28, 50, 54</sup> seen at 819 cm<sup>-1</sup> increased in intensity after the treatment with **1** in Ar atmosphere, relative to other Raman peaks (**Figure 4c**), suggesting a filling of oxygen vacancies at the μ<sub>2</sub>-O position with O atoms derived from **1**. Upon this treatment, a red shift of plasmonic wavelength was observed in UV-vis-NIR spectrum, while the crystal structure remained unchanged (see **Figure S11**). These results indicate re-oxidation of the reduced Mo species and a decreased concentration of dopant levels by the reaction with **1** due to a filling of oxygen vacancies with O atoms derived from **1**. Furthermore, to track the progress of the deoxygenation reaction, *in-situ* FTIR measurement using dimethyl sulfoxide (DMSO) as a probe molecule was performed at room temperature in a continuous flow of H<sub>2</sub> (**Figure S12**). An intense IR band assignable to strongly chemisorbed DMSO molecule was observed on Pt/H<sub>x</sub>MoO<sub>3-y</sub>(200), while it was hardly observed on Pt/SiO<sub>2</sub>, proving the existence of strong adsorption sites on H<sub>x</sub>MoO<sub>3-y</sub> surface. This IR band was gradually decreased in intensity after the exposure to H<sub>2</sub> gas flow, clearly demonstrating the deoxygenation of sulfoxide occurring on H<sub>x</sub>MoO<sub>3-y</sub> surface (not on Pt NPs surface) using H<sub>2</sub> molecule as a reductant.

Based on these experimental results, the reaction pathway for the deoxygenation of sulfoxide over Pt/H<sub>x</sub>MoO<sub>3-y</sub> hybrid is proposed as illustrated in **Scheme 2**; a heavily-doped molybdenum oxide maintains massive oxygen vacancies, which are generated in MoO<sub>3</sub> matrices via a H-spillover process (step 1 and 2). The thus formed oxygen vacancies, mainly involving μ<sub>2</sub>-bridging oxygen sites, with positive charges effectively trap the negatively-charged O atom of sulfoxide (step 3) and act as the main active sites to directly deoxygenate sulfoxides to sulfides, which results in a filling of oxygen vacancies and a concomitant oxidation of adjacent Mo species (step 4). Afterwards, the oxidized species readily react with the active H atoms, which are dissociated on Pt NPs, to regenerate the original active species. Thus, massive oxygen vacancies and the reversible redox property of Mo atoms in H<sub>x</sub>MoO<sub>3-y</sub> can provide an effective catalytic system for this reaction under mild conditions.

**Scheme 2.** Possible reaction pathway of the deoxygenation of sulfoxide over Pt/H<sub>x</sub>MoO<sub>3-y</sub> hybrid catalyst using molecular H<sub>2</sub> as a reductant



**Plasmon-driven activity enhancement.** Intriguingly, under the irradiation of visible light ( $\lambda > 420$  nm,  $I = 19.6$  mW/cm<sup>2</sup>), a significant improvement of catalytic efficiency was observed over Pt/H<sub>x</sub>MoO<sub>3-y</sub>(200) catalyst, giving a two-fold faster reaction rate relative to dark condition (**Figure 5a**). Such an activity enhancement was not observed on non-plasmonic catalysts such as Pt/SiO<sub>2</sub>, Pt/WO<sub>3</sub>, and Pt/MoO<sub>2</sub> upon the exposure to visible light (**Figure 5b**). The catalytic activity increased in proportion to the intensity of the incident light (**Figure 5c**). The catalytic reactions were also performed with LED lamp irradiation, including blue ( $\lambda_{\text{max}} = 470$  nm), green ( $\lambda_{\text{max}} = 530$  nm), and red LED ( $\lambda_{\text{max}} = 650$  nm). The degree of activity increase (normalized by each light intensity) was nearly consistent with the absorption spectrum of Pt/H<sub>x</sub>MoO<sub>3-y</sub>(200) measured by UV-vis-NIR spectroscopy (**Figure 5d**), demonstrating that the activity enhancement is driven by plasmonic effect of hydrogen molybdenum bronze. To the best of our knowledge, this is the first report on plasmon-induced activity enhancement in the deoxygenation reaction.




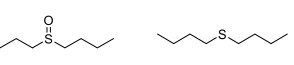


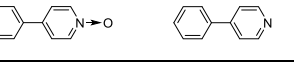

**Figure 5.** (a) Time course is 470 nm) over Pt/H<sub>x</sub>MoO<sub>3-y</sub>(200) catalyst in the dark or under visible light ( $\lambda > 420$  nm,  $I = 19.6$  mW/cm<sup>2</sup>) irradiation conditions. (b) Comparison of catalytic activities over various catalysts in the dark or under visible light irradiation conditions (reduction Temp. = 200 °C). (c) Catalytic activity dependence on the intensity of visible light over Pt/H<sub>x</sub>MoO<sub>3-y</sub>(200) catalyst. (d) The increased yield of 2 as a function of the wavelength by LED irradiation over Pt/H<sub>x</sub>MoO<sub>3-y</sub>(200) catalyst (left axis) and its Kubelka-Munk function (right axis). Reaction conditions are the same as those described in Figure 3.

The origin of the visible light-induced activity enhancement in plasmonic semiconductor materials may involve i) photothermal effect, ii) interfacial charge transfer mechanism or iii) electric near-field enhancement (ENFE) effect.<sup>5</sup> To eliminate the contribution of the photothermal effect, a control experiment at 40 °C was performed in the dark. The yield of 2 after 1 h of reaction in the dark at 40 °C was 38%, which was higher than the yield obtained in the dark at near room temperature (30% at 30 °C) but was apparently lower than that attained under light irradiation (50% at room temperature) (**Figure 5c**). In fact, the temperature

of the reaction suspension was found to increase by only ca. 0.5 °C under visible light irradiation, thereby the contribution of photothermal effect can be disregarded in the present catalytic system. The negligible temperature increase during the light irradiation may be explained by the high non-polarity of toluene used as a medium, which is far less susceptible to SPR effect relative to other polar media. In the plasmonic hybrid system, hot electrons produced by plasmonic SPR are, in general, believed to be transferred to the contiguous metal NPs to create negatively charged NPs, which accelerates specific catalytic reactions (interfacial charge transfer)<sup>13, 22, 30</sup>. In the case of Pt/H<sub>x</sub>MoO<sub>3-y</sub> catalytic system, Pt NPs anchored on plasmonic molybdenum oxide act as dissociation sites for H<sub>2</sub>; however, kinetic analysis revealed that the reaction rate is independent from partial pressure of H<sub>2</sub> gas both in the dark and under visible light irradiation conditions (reaction order was close to zero, see **Figure S13**), thereby discounting the positive involvement of charge transfer in the present catalytic system. Therefore, we speculated that the enhanced catalytic activity is attributed to the electric near-field enhancement (ENFE) effect of hydrogen molybdenum bronze. To verify this hypothesis, *in-situ* FTIR measurement using DMSO was performed at room temperature under visible light irradiation (**Figure S14**). A gradual shift of the IR band assignable to S=O bond of chemisorbed DMSO toward lower wavenumbers was unambiguously observed upon the irradiation of visible light. This result suggests that the electric near-field induced around the surface of hydrogen molybdenum bronze owing to the SPR effect upon visible light irradiation facilitates the activation of sulfoxide by stretching the S=O bond. The stretched sulfoxide displays a larger molecular polarity and can be deoxygenated more efficiently by active centers, thus accelerating the reaction.<sup>55</sup>

**Table 2. Scope of substrates in the deoxygenation of sulfoxides and pyridine N-oxides with 1 atm H<sub>2</sub> at room temperature over Pt/H<sub>x</sub>MoO<sub>3-y</sub>(200) catalyst<sup>a</sup>**

| Entry | Substrate | Product | Time (h) | Conv. <sup>b</sup> (%) | Sel. <sup>b</sup> (%) |
|-------|-----------|---------|----------|------------------------|-----------------------|
| 1     |           |         | 3        | >99 (67)               | >99 (>99)             |
| 2     |           |         | 2        | >99 (54)               | >99 (>99)             |
| 3     |           |         | 4        | >99 (60)               | >99 (>99)             |
| 4     |           |         | 3        | >99 (66)               | >99 (>99)             |
| 5     |           |         | 3        | >99 (66)               | >99 (>99)             |
| 6     |           |         | 2        | >99 (71)               | >99 (>99)             |
| 7     |           |         | 6        | >99 (72)               | >99 (>99)             |

|                 |   |    |             |              |
|-----------------|---|----|-------------|--------------|
| 8               |   | 2  | >99<br>(44) | >99<br>(>99) |
| 9               |  | 24 | >99<br>(69) | >99<br>(>99) |
| 10 <sup>c</sup> |  | 2  | >99<br>(47) | >99<br>(>99) |
| 11 <sup>c</sup> |  | 3  | >99<br>(85) | >99<br>(>99) |
| 12 <sup>d</sup> |  | 5  | >99<br>(78) | >99<br>(>99) |
| 13 <sup>d</sup> |  | 3  | >99<br>(75) | >99<br>(>99) |

<sup>a</sup>Reaction conditions: catalyst (Pt/H<sub>x</sub>MoO<sub>3-y</sub>(200), 0.05 g), sulfoxide (0.2 mmol), toluene (10 mL), room temperature, H<sub>2</sub> bubbling (10 mL/min), visible light ( $\lambda > 420$  nm) emitted from 500 W Hg-Xe short arc lamp using a cut-off filter. <sup>b</sup>Values in parentheses are those obtained in the dark condition. <sup>c</sup>pyridine *N*-oxide (1.0 mmol), acetonitrile was used as a solvent. <sup>d</sup>pyridine *N*-oxide (0.5 mmol), acetonitrile was used as a solvent.

Pt/H<sub>x</sub>MoO<sub>3-y</sub> hybrid provided excellent selectivity for the deoxygenation of other sulfoxides (Table 2). In all cases, drastically improved catalytic efficiencies were obtained under visible light irradiation relative to dark condition. A variety of aromatic and aliphatic sulfoxides were converted to the corresponding sulfides with excellent yields (entries 1–9), and pyridine *N*-oxides were also successfully deoxygenated, providing the corresponding pyridines (entry 10–13) under the irradiation of visible light. In addition, the structural and optical stability upon the catalytic use was examined by XRD and UV-vis-NIR measurements (Figure S11). Although a plasmonic wavelength caused a red-shift from 556 to 660 nm due to the decreased carrier concentration in the MoO<sub>3</sub> matrix associated with the partial filling of oxygen vacancies, the crystalline structure (H<sub>0.9</sub>MoO<sub>3</sub> phase) remained unchanged during the reaction. With specific treatment to regenerate the oxygen vacancies, Pt/H<sub>x</sub>MoO<sub>3-y</sub> hybrid could be reused over multiple catalytic runs without significant loss of catalytic performances (Figure S15). These results demonstrate the potential application of the plasmonic molybdenum oxide hybrid as an efficient and stable deoxygenation catalyst.

### 3. CONCLUSIONS

In conclusion, efficient catalytic deoxygenation of sulfoxides was demonstrated using plasmonic H<sub>x</sub>MoO<sub>3-y</sub> coupled with Pt NPs. Notably, this deoxygenation proceeds under mild reaction conditions (using 1 atm H<sub>2</sub> and at room temperature) and is drastically accelerated under visible light irradiation relative to dark condition. Comprehensive analyses revealed that the massive oxygen vacancies, reversible redox property of Mo atoms and strong plasmonic absorption of hydrogen-doped molybdenum oxides play crucial roles in this reaction. Such an extraordinary performance presents a great opportunity for utilizing degenerately doped plasmonic molybdenum oxide as a light-harvesting

platform in heterogeneous catalysis, which can boost diverse selective organic transformations under solar light.

### 4. EXPERIMENTAL SECTION

**Materials.** Hexaammonium heptamolybdate tetrahydrate ((NH<sub>4</sub>)<sub>6</sub>Mo<sub>7</sub>O<sub>24</sub> · 4H<sub>2</sub>O; 99.0%), ruthenium (III) chloride hydrate (RuCl<sub>3</sub> · xH<sub>2</sub>O), and tungsten(VI) oxide (WO<sub>3</sub>) were purchased from Wako Pure Chemical Industries, Ltd. Potassium tetrachloroplatinate(II) (K<sub>2</sub>PtCl<sub>4</sub>), disodium tetrachloropalladate (II) (Na<sub>2</sub>PdCl<sub>4</sub>), vanadium(V) oxide (V<sub>2</sub>O<sub>5</sub>), urea (99.0%), and other commercially available chemical reagents for catalytic tests were purchased from Nacalai Tesque, Inc. Fumed silica (SiO<sub>2</sub>) and molybdenum(IV) oxide (MoO<sub>2</sub>) as catalyst supports were purchased from Sigma-Aldrich Co.  $\gamma$ -Al<sub>2</sub>O<sub>3</sub> (JRC-ALO-4) as a catalyst support was supplied from the Catalysis Society of Japan. All chemicals were used as received without further purification.

**Synthesis of Pt/H<sub>x</sub>MoO<sub>3-y</sub> hybrid.** The plasmonic hydrogen molybdenum bronzes coupled with Pt NPs (Pt/H<sub>x</sub>MoO<sub>3-y</sub>) were prepared by a two-step synthetic process.<sup>22</sup> Firstly,  $\alpha$ -MoO<sub>3</sub> was prepared by thermal decomposition of (NH<sub>4</sub>)<sub>6</sub>Mo<sub>7</sub>O<sub>24</sub> · 4H<sub>2</sub>O at 500 °C for 4 h in air with the ramping rate of 1 °C/min. Pt/MoO<sub>3</sub> was obtained by a precipitation method using urea as a precipitant;  $\alpha$ -MoO<sub>3</sub> (1.0 g) was dispersed in 100 mL of distilled water containing 1.5 mL of K<sub>2</sub>PtCl<sub>4</sub> solution (35 mM). To this suspension, 0.2 g of urea as a precipitation reagent was added, followed by vigorous stirring for 6 h at 95 °C to precipitate Pt<sup>2+</sup> ions. The obtained slurry was centrifuged, washed with deionized water and ethanol and then vacuum-dried to yield as-prepared Pt/MoO<sub>3</sub>. Subsequently, hydrogen reduction of Pt/MoO<sub>3</sub> was conducted in a flow of H<sub>2</sub> (20 mL/min) for 30 min at ambient pressure (1 bar) with a heating rate of 5 °C/min to yield Pt/H<sub>x</sub>MoO<sub>3-y</sub>(*T*) (*T* represents the reduction temperature (°C)) as a dark blue powder. 30 min of H<sub>2</sub> reduction was enough to yield Pt/H<sub>x</sub>MoO<sub>3-y</sub>(*T*) and no further significant optical and compositional variation was observed even though the reduction time was extended. Pt loading was determined to be 0.49 wt% by inductively coupled plasma (ICP) analysis. This is the Pt loading optimized in the preliminary study (for the effect of Pt loading, see Figure S16).

**Synthesis of reference catalyst.** Reference catalysts used for the deoxygenation of sulfoxides were prepared by a similar procedure mentioned above. Pd/H<sub>x</sub>MoO<sub>3-y</sub> and Ru/H<sub>x</sub>MoO<sub>3-y</sub> hybrids were prepared using Na<sub>2</sub>PdCl<sub>4</sub> and RuCl<sub>3</sub> · xH<sub>2</sub>O as precursors instead of K<sub>2</sub>PtCl<sub>4</sub>, respectively, and by reducing in a flow of H<sub>2</sub> at 200 °C for 30 min. Pd and Ru loadings were determined to be 0.59 and 0.66 wt%, respectively, by inductively coupled plasma (ICP) analysis. Supported Pt NP catalysts (Pt/WO<sub>3</sub>, Pt/MoO<sub>2</sub>, Pt/SiO<sub>2</sub>, and Pt/Al<sub>2</sub>O<sub>3</sub>) were also prepared by using the corresponding oxide as a catalyst support instead of  $\alpha$ -MoO<sub>3</sub>, and by reducing in a flow of H<sub>2</sub> at 200 °C for 30 min. Pt loading was fixed to be 0.5 wt%. Specific surface area (*S*<sub>BET</sub>) was calculated to be 4.2 m<sup>2</sup>/g (Pt/WO<sub>3</sub>), 5.8 m<sup>2</sup>/g (Pt/MoO<sub>2</sub>), 222 m<sup>2</sup>/g (Pt/SiO<sub>2</sub>), and 193 m<sup>2</sup>/g (Pt/Al<sub>2</sub>O<sub>3</sub>), respectively.

**Characterization.** Powder X-ray diffraction (XRD) patterns were recorded using a Rigaku Ultima IV diffractometer with Cu K $\alpha$  radiation ( $\lambda = 1.5406$  Å, 40 kV–40 mA). UV-vis-NIR diffuse reflectance spectra were collected on a Shimadzu UV-2600 recording spectrophotometer equipped with an integrat-



ing sphere at room temperature. BaSO<sub>4</sub> was used as a reference and the absorption spectra were obtained using the Kubelka-Munk function. X-ray photoelectron spectroscopy (XPS) measurements were carried out on a Shimadzu ESCA-3400 photoelectron spectrometer with a Mg K $\alpha$  radiation (1253.6 eV) X-ray source at a pressure lower than 10<sup>-6</sup> Pa. The binding energy was calibrated with the adventitious carbon (C 1s) peak at 284.5 eV. Transmission electron microscopy (TEM) images were obtained with a Hitachi H-800 electron microscope operated at 200 kV. Specific surface area ( $S_{\text{BET}}$ ) and total pore volume ( $V_{\text{total}}$ ) was determined using the N<sub>2</sub> adsorption isotherm data collected at -196 °C using a BELSORP-max system (MicrotracBEL Corp.).  $S_{\text{BET}}$  was determined by the BET (Brunauer-Emmett-Teller) method by using adsorption data ranging from  $p/p_0 = 0.05$  to 0.30. Raman spectra were obtained with a Laser Analyzer of RAMAN-II (Nano Photo company) with a narrow linewidth diode laser at 532 nm and laser intensity of 2 mW. Electron spin resonance (ESR) spectra were acquired on a JEOL RESONANCE JES-TE200 spectrometer at room temperature with a Klystron frequency of 9.45 GHz at 1.2 mW power. For ESR spectrum taken under dehydrated conditions, as-prepared Pt/MoO<sub>3</sub> sample was reduced at 200 °C for 30 min in a flow of H<sub>2</sub> and was transferred to a quartz-made tube without exposure to the air prior to analysis. The signal intensities were normalized with respect to a MnO marker.

**Thermogravimetric analysis.** The concentrations of hydrogen atoms and oxygen vacancies ( $O_v$ ) introduced in MoO<sub>3</sub> matrices were quantified from the thermogravimetric (TG) data measured on a Rigaku Thermo plus EVO2 under a flow of N<sub>2</sub> and air, respectively. The as-prepared Pt/MoO<sub>3</sub> (10 mg) mounted on an alumina pan were reduced at desired temperature ( $T = 40, 100, \text{ and } 200$  °C) in a flow of H<sub>2</sub> for 30 min to yield Pt/H<sub>x</sub>MoO<sub>3-y</sub>( $T$ ), and subsequently cooled to 40 °C. TG profiles were collected by heating the samples from 40 to 450 °C with a heating rate of 10 °C/min under a 100 mL/min flow of either N<sub>2</sub> or bone-dry air.

**Catalytic test:** In a typical procedure, as-synthesized Pt/MoO<sub>3</sub> catalyst (0.05 g) was placed in a Pyrex glass tube, followed by H<sub>2</sub> reduction at 200 °C for 30 min. After cooling to ambient temperature, 10 mL of toluene solution containing sulfoxides (0.2 mmol) was injected into the reactor through a rubber septum by using a syringe. The reaction was performed in a continuous flow of atmospheric pressure of H<sub>2</sub> (10 mL/min) at room temperature (20 $\pm$ 3 °C) with magnetic stirring in the dark or under visible light irradiation ( $\lambda > 420$  nm) conditions. A 500 W Hg-Xe short arc lamp (SAN-EI ELECTRIC XEF-501S) with a 420 nm cutoff filter was used to simulate visible light ( $\lambda > 420$  nm,  $I = 19.6$  mW/cm<sup>2</sup>). The reaction was also carried out upon irradiation by LED light (blue light:  $\lambda = 470$  nm,  $I = 33.3$  mW/cm<sup>2</sup>; green light:  $\lambda = 530$  nm,  $I = 17.0$  mW/cm<sup>2</sup>; red light:  $\lambda = 650$  nm,  $I = 23.5$  mW/cm<sup>2</sup>). At given time intervals, 500  $\mu$ L of the suspension was retrieved, filtered and analysed by gas chromatograph (Shimadzu GC-2010) with a flame ionization detector (FID) equipped with a capillary column (HiCap-CBP10; 0.22 mm  $\times$  25 m) using biphenyl as an internal standard.

## ASSOCIATED CONTENT

### Supporting Information.

This Supporting Information is available free of charge via the Internet at <http://pubs.acs.org>.

Experimental procedures for TPR, TPD, *in-situ* XAFS, *in-situ* FTIR measurements, TPR profiles (Figure S1), XRD patterns and UV-vis-NIR spectra (Figure S2), Mo 3d and O 1s XPS spectra (Figure S3, Table S1), *in-situ* XAFS spectra (Figure S4), TEM image and Pt 4f XPS spectra (Figure S5), NH<sub>3</sub>-TPD profiles (Figure S6), FT-Raman spectra (Figure S7), TG profiles (Figure S8), effect of solvent (Figure S9), relationship between activity and some compositional parameters of catalysts (Figure S10), XRD patterns and UV-vis-NIR spectra of spent catalyst (Figure S11), *in-situ* FTIR spectra in H<sub>2</sub> flow (Figure S12), effect of H<sub>2</sub> partial pressure on the reaction rate (Figure S13), *in-situ* FTIR spectra under visible light (Figure S14), reusability test (Figure S15), effect of Pt loading (Figure S16) and summary of XPS analysis (Table S1) (PDF)

## AUTHOR INFORMATION

### Corresponding Author

\*yamashita@mat.eng.osaka-u.ac.jp

### Notes

The authors declare no competing financial interest.

## ACKNOWLEDGMENT

This work was supported by a Grant-in-Aid from the Frontier Research Base for Global Young Researchers, Osaka University, and the Grant-in-Aid for Scientific Research (KAKENHI) from JSPS (no. 26620194, 26220911). Part of this work was performed under the management of "Elements Strategy Initiative for Catalysts & Batteries (ESICB)" supported by MEXT, Japan. The synchrotron radiation experiments for XAFS measurements were performed at the BL01B1 beam line in SPring-8 with the approval from JASRI (no. 2016A1057, 2017A1063).

## REFERENCES

1. Linic, S.; Christopher, P.; Ingram, D. B. *Nat. Mater.* **2011**, *10* (12), 911-21.
2. Clavero, C. *Nat. Photonics* **2014**, *8* (2), 95-103.
3. Peiris, S.; McMurtrie, J.; Zhu, H.-Y. *Catal. Sci. Technol.* **2016**, *6* (2), 320-338.
4. He, R.; Wang, Y. C.; Wang, X.; Wang, Z.; Liu, G.; Zhou, W.; Wen, L.; Li, Q.; Wang, X.; Chen, X.; Zeng, J.; Hou, J. G. *Nat. Commun.* **2014**, *5*, 4327.
5. Cheng, H.; Fuku, K.; Kuwahara, Y.; Mori, K.; Yamashita, H. *J. Mater. Chem. A* **2015**, *3* (10), 5244-5258.
6. Zhang, X.; Ke, X.; Zhu, H. *Chem. Eur. J.* **2012**, *18* (26), 8048-8056.
7. Ke, X.; Sarina, S.; Zhao, J.; Zhang, X.; Chang, J.; Zhu, H. *Chem. Commun.* **2012**, *48* (29), 3509-3511.
8. Zhu, H.; Ke, X.; Yang, X.; Sarina, S.; Liu, H. *Angew. Chem. Int. Ed.* **2010**, *49* (50), 9657-9661.
9. Mori, K.; Verma, P.; Hayashi, R.; Fuku, K.; Yamashita, H. *Chem. Eur. J.* **2015**, *21* (33), 11885-93.
10. Christopher, P.; Xin, H.; Linic, S. *Nat. Chem.* **2011**, *3* (6), 467-472.
11. Wang, F.; Li, C.; Chen, H.; Jiang, R.; Sun, L. D.; Li, Q.; Wang, J.; Yu, J. C.; Yan, C. H. *J. Am. Chem. Soc.* **2013**, *135* (15), 5588-5601.
12. Sarina, S.; Zhu, H.; Jaatinen, E.; Xiao, Q.; Liu, H.; Jia, J.; Chen, C.; Zhao, J. *J. Am. Chem. Soc.* **2013**, *135* (15), 5793-5801.
13. Verma, P.; Kuwahara, Y.; Mori, K.; Yamashita, H. *J. Mater. Chem. A* **2016**, *4* (26), 10142-10150.

14. Della Gaspera, E.; Chesman, A. S. R.; van Embden, J.; Jasieniak, J. J. *ACS Nano* **2014**, *8* (9), 9154-9163.
15. Johns, R. W.; Bechtel, H. A.; Runnerstrom, E. L.; Agrawal, A.; Lounis, S. D.; Milliron, D. J. *Nat. Commun.* **2016**, *7*, 11583.
16. Comin, A.; Manna, L. *Chem. Soc. Rev.* **2014**, *43*, 3957-3975.
17. Liu, X.; Swihart, M. T. *Chem. Soc. Rev.* **2014**, *43* (11), 3908-20.
18. Li, Y.; Cheng, J.; Liu, Y.; Liu, P.; Cao, W.; He, T.; Chen, R.; Tang, Z. *J. Phys. Chem. C* **2017**, *121* (9), 5208-5214.
19. Luther, J. M.; Jain, P. K.; Ewers, T.; Alivisatos, A. P. *Nat. Mater.* **2011**, *10* (5), 361-6.
20. Kriegel, I.; Scotognella, F.; Manna, L. *Physics Reports* **2017**, *674*, 1-52.
21. Hu, X. K.; Qian, Y. T.; Song, Z. T.; Huang, J. R.; Cao, R.; Xiao, J. Q. *Chem. Mater.* **2008**, *20*, 1527-1533.
22. Cheng, H.; Wen, M.; Ma, X.; Kuwahara, Y.; Mori, K.; Dai, Y.; Huang, B.; Yamashita, H. *J. Am. Chem. Soc.* **2016**, *138* (29), 9316-24.
23. Cheng, H.; Kamegawa, T.; Mori, K.; Yamashita, H. *Angew. Chem. Int. Ed.* **2014**, *53* (11), 2910-29.
24. Alsaif, M. M. Y. A.; Latham, K.; Field, M. R.; Yao, D. D.; Medehkar, N. V.; Beane, G. A.; Kaner, R. B.; Russo, S. P.; Ou, J. Z.; Kalantar-zadeh, K. *Adv. Mater.* **2014**, *26*, 3931-3937.
25. Alsaif, M. M. Y. A.; Chrimes, A. F.; Daeneke, T.; Balendhran, S.; Bellisario, D. O.; Son, Y.; Field, M. R.; Zhang, W.; Nili, H.; Nguyen, E. P.; Latham, K.; van Embden, J.; Strano, M. S.; Ou, J. Z.; Kalantar-zadeh, K. *Adv. Funct. Mater.* **2016**, *26* (1), 91-100.
26. Balendhran, S.; Deng, J.; Ou, J. Z.; Walia, S.; Scott, J.; Tang, J.; Wang, K. L.; Field, M. R.; Russo, S.; Zhuiykov, S.; Strano, M. S.; Medhekar, N.; Sriram, S.; Bhaskaran, M.; Kalantar-Zadeh, K. *Adv. Mater.* **2013**, *25*, 109-114.
27. Tan, X.; Melkersson, J.; Wu, S.; Wang, L.; Zhang, J. *ChemPhysChem* **2016**, *17* (17), 2630-9.
28. Liu, W.; Xu, Q.; Cui, W.; Zhu, C.; Qi, Y. *Angew. Chem. Int. Ed.* **2017**, *56* (6), 1600-1604.
29. Yin, H.; Kuwahara, Y.; Mori, K.; Cheng, H.; Wen, M.; Yamashita, H. *J. Mater. Chem. A* **2017**, *5* (19), 8946-8953.
30. Cheng, H.; Qian, X.; Kuwahara, Y.; Mori, K.; Yamashita, H. *Adv. Mater.* **2015**, *27* (31), 4616-4621.
31. Guan, J.; Peng, G.; Cao, Q.; Mu, X. *J. Phys. Chem. C* **2014**, *118* (44), 25555-25566.
32. Prasomsri, T.; Nimmanwudipong, T.; Román-Leshkov, Y. *Energy Environ. Sci.* **2013**, *6* (6), 1732-1738.
33. Sousa, S. C. A.; Fernandes, A. C. *Coord. Chem. Rev.* **2015**, *284*, 67-92.
34. Madesclaire, M. *Tetrahedron* **1988**, *44* (21), 6537-6580.
35. Arnáiz, F.; Sanz, R.; Escribano, J.; Aguado, R.; Pedrosa, M. *Synthesis* **2004**, *2004* (10), 1629-1632.
36. Fernandes, A. C.; Romão, C. C. *Tetrahedron Lett.* **2007**, *48* (52), 9176-9179.
37. Mikami, Y.; Noujima, A.; Mitsudome, T.; Mizugaki, T.; Jitsukawa, K.; Kaneda, K. *Chem. Eur. J.* **2011**, *17* (6), 1768-72.
38. Takahashi, Y.; Mitsudome, T.; Mizugaki, T.; Jitsukawa, K.; Kaneda, K. *Chem. Lett.* **2014**, *43* (4), 420-422.
39. Ogura, K.; Yamashita, M.; Tsuchihashi, G. *Synthesis* **1975**, *1975*, 385-387.
40. Touchy, A. S.; Hakim Siddiki, S. M. A.; Onodera, W.; Kon, K.; Shimizu, K.-i. *Green Chem.* **2016**, *18* (8), 2554-2560.
41. Uematsu, T.; Ogasawara, Y.; Suzuki, K.; Yamaguchi, K.; Mizuno, N. *Catal. Sci. Technol.* **2017**, *7* (9), 1912-1920.
42. Mitsudome, T.; Takahashi, Y.; Mizugaki, T.; Jitsukawa, K.; Kaneda, K. *Angew. Chem. Int. Ed.* **2014**, *53* (32), 8348-8351.
43. Birtill, J. J.; Dickens, P. G. *Mat. Res. Bul.* **1978**, *13*, 311-316.
44. Pichat, P.; Mozzanega, M.-N.; Hoang-Van, C. *J. Phys. Chem.* **1988**, *92*, 467-470.
45. Adams, S. J. *Solid State Chem.* **2000**, *149*, 75-87.
46. Bräida, B.; Adams, S.; Canadell, E. *Chem. Mater.* **2005**, *17*, 5957-5969.
47. Kim, H. S.; Cook, J. B.; Lin, H.; Ko, J. S.; Tolbert, S. H.; Ozolins, V.; Dunn, B. *Nat. Mater.* **2017**, *16* (4), 454-460.
48. Borgschulte, A.; Sambalova, O.; Delmelle, R.; Jenatsch, S.; Hany, R.; Nuesch, F. *Sci. Rep.* **2017**, *7*, 40761.
49. Lei, Y.-H.; Chen, Z.-X. *J. Phys. Chem. C* **2012**, *116* (49), 25757-25764.
50. Ou, J. Z.; Campbell, J. L.; Yao, D.; Wlodarski, W.; Kalantar-zadeh, K. *J. Phys. Chem. C* **2011**, *115*, 10757-10763.
51. Sotani, N.; Eda, K.; Sadamatu, M.; Takagi, S. *Bull. Chem. Soc. Jpn.* **1989**, *62*, 903-907.
52. Seshadri, K. S.; Petrakis, I. J. *Catal.* **1973**, *30*, 195-203.
53. Watson, R. B.; Ozkan, U. S. *J. Phys. Chem. B* **2002**, *106*, 6930-6941.
54. Eda, K. *J. Solid State Chem.* **1992**, *98*, 350-357.
55. Zhang, X.; Ke, X.; Du, A.; Zhu, H. *Sci. Rep.* **2014**, *4*, 3805.

## Table of Contents (TOC)

